



Power Electronic Systems
Laboratory

© 2019 IEEE

Proceedings of the 22nd International Conference on Electrical Machines and Systems (ICEMS 2019),
Harbin, China, August 11-14, 2019

Optimization and Calorimetric Analysis of Axial Flux Permanent Magnet Motor for Implantable Blood Pump Assisting Fontan Circulation

E. Hubmann,
D. Bortis,
M. Flankl,
M. Granegger,
M. Hübler,
J. W. Kolar

Personal use of this material is permitted. Permission from IEEE must be obtained for all other uses, in any current or future media, including reprinting/republishing this material for advertising or promotional purposes, creating new collective works, for resale or redistribution to servers or lists, or reuse of any copyrighted component of this work in other works.



Eidgenössische Technische Hochschule Zürich
Swiss Federal Institute of Technology Zurich

Optimization and Calorimetric Analysis of Axial Flux Permanent Magnet Motor for Implantable Blood Pump Assisting the Fontan Circulation

E. J. Hubmann*, D. Bortis*, M. Flankl *, J. W. Kolar*, M. Granegger †, and M. Hübler‡

*Power Electronic Systems Laboratory, ETH Zurich, Switzerland, hubmann@lem.ee.ethz.ch

†Biofluid Mechanics Laboratory, Charité - Universitätsmedizin Berlin, Germany

‡Pediatric Heart Center, Department of Surgery, University Children's Hospital Zurich, Switzerland

Abstract—This paper presents a constrained optimization and calorimetric experimental analysis of low torque (2.2 mNm) axial flux permanent magnet motors with small active rotor surface area (1.4 cm²) with the aim to drive an implantable blood pump to support patients with a Fontan circulation. Till today, no such treatment option is clinically available, despite the urgent need. For a previously presented implantable blood pump concept, in this paper now the corresponding motors are optimized concerning efficiency and power density, where e.g. the optimal permanent magnet and back-iron height of the rotor or the optimal pole pair number and tooth height of the stator are determined. Afterwards, the different motor prototypes are realized, tested and compared to each other. Besides the implant size also the generated motor losses are very crucial, since the local temperature increase of the blood and surrounding tissue must always be kept below 2 °C. However, as will be shown in this paper, due to the fact that the low torque of the motors cannot be separated from the test-bench bearing friction with conventional torque sensors, a sophisticated calorimetric test bench to accurately measure the motor losses is needed.

Index Terms—axial flux permanent magnet motor, implantable blood pump, Fontan assist, calorimetric

I. INTRODUCTION

Newborns suffering from a congenital heart defect with an underdeveloped ventricle got a chance to reach adulthood with the invention of the Fontan surgery [1], [2]. The step-wise Fontan procedure converts the cardiovascular system into a univentricular circulation. There, venous blood is directly guided to the lungs without the interposition of a sub-pulmonary ventricle via the surgically formed cross shaped total cavopulmonary connection (TCPC) [3], where the remaining single ventricle pumps the blood from the lungs to the systemic circulation as shown in **Fig. 1**. 25 years after successful completion of the Fontan circulation, survival and freedom from Fontan failure rate are reported as 83% and 56% respectively [4], indicating the urgent medical need for a novel treatment option. While 4–8 per 10'000 children are born with an underdeveloped ventricle [5], the lifetime risk in general for heart failure is one in five, but this occurs mostly in patients older than 65 years [6]. For biventricular patients, the treatment of heart failure with implantable left ventricular assist devices (LVADs) constitutes the state of the art, with several commercially available devices such as HeartMate II and III (Abbott), HVAD (Medtronic) and INCOR (Berlin Heart). Despite promising survival rates, the success of this therapy is tainted by device related severe adverse events as right heart failure, bleeding, stroke, aortic insufficiency and driveline infections [7].

The lack of treatment options in case of a single ventricle has led to research activity in the field of assist devices for Fontan patients, with the aim to compensate for the underdeveloped ventricle with a pumping device [8]. However, compared to the state of the art of LVADs designed for adults, a long-term treatment solution for Fontan patients

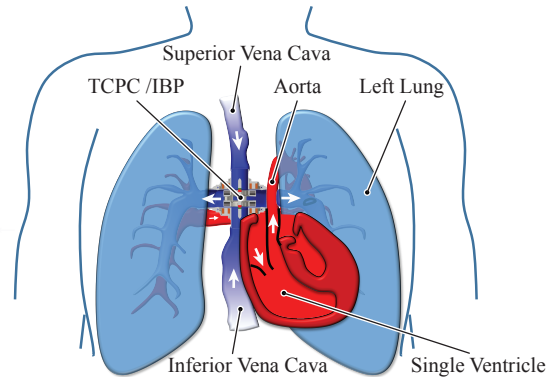


Fig. 1. Fontan circulation with surgically formed cross shaped total cavopulmonary connection (TCPC), where the TCPC can be replaced by an implantable blood pump (IBP) system.

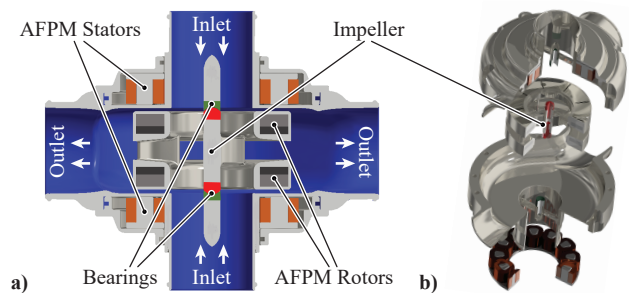


Fig. 2. a) 2D-CAD section through the implantable blood pump (IBP) and b) CAD rendering of the pump according to [9] with newly optimized axial flux permanent magnet (AFPM) motors.

needs to show less adverse events, smaller size for small patients and a specific design for the Fontan circulation. So far, no such long-term Fontan assist device is clinically available, presumably due to the lack of technological breakthrough, comparatively small market, high economic risk and large necessary investments for protracted development and approval processes. Therefore at the University Children's Hospital Zurich a project was launched to address the need for improved Fontan assist device technology [9]. The substitution of the surgically created TCPC is considered to be a promising implant location, which keeps the added volume minimal (cf. **Fig. 1**). This implies that the pump features two inlets and two outlets with location corresponding to the anatomy of the pulmonary arteries and venae cavae. In [9], a novel continuous flow implantable blood pump (IBP) concept was presented, with a symmetric design having axial inflow from both venae cavae and radial outflow into the pulmonary arteries as shown in **Fig. 2**.

The symmetric turbomachinery design was optimized with computational fluid dynamics (CFD) indicating favourable hydraulic properties, lower shear loading on the blood compared to today's LVADs, and high hydraulic efficiency. Good washout was achieved by large clearances between impeller and housing to prevent thrombus formation. In addition, an axial arrangement of two permanent magnet synchronous machines was proposed to provide redundantly the impeller torque. The axially symmetric impeller comprises the permanent magnets (PM) and the rotor back-irons, while two stators are arranged axially displaced around the two pump inlets (cf. Fig. 2). In [9], the machine concept was presented, but no motor optimization, hardware realization and experimental investigation were performed, which is now carried out in this paper. The main focus is laid on the compact realization of the stator due to the limited available space and on achieving a high motor efficiency (Pareto curve), such that the local temperature increase (hot-spot) of the blood and surrounding tissue can always be kept below 2°C (ISO 14708-1). In [9], it was shown that for this particular pump concept, where at full load operation a rotational speed of 5500 rpm and a torque of 2.2 mNm are achieved, 2.5 W of losses per motor can be cooled by the blood stream without violating the ISO 14708-1 standard and the local hot-spot at the housing wall adjacent to the stators will lead to a blood temperature increase of around 1.5°C . Furthermore, challenges lie in the relatively large magnetic air gap given by the housing walls and the clearance between impeller and housing, leading to a high amount of leakage flux. **Section II** therefore deals first with the motor optimization, i.e. the optimization of the number of pole pairs, division into magnet and iron volume, the height of the stator teeth, the division into copper and iron volumes as well as the selection of core materials. In addition, based on the hemodynamic boundary conditions and fluid dynamic analyses derived in [9], the motor speed and torque requirements are directly given as shown in Fig. 3.

For the proposed pump concept, the speed reaches up to 5500 rpm and leads to a very low torque requirement of 2.2 mNm per motor as compared to applications for an LVAD [10] with 12 mNm or a total artificial heart [11] with 80 mNm. Such low torques, however, make the metrological verification of the machine optimization challenging, e.g. because the load from the test-bench bearings is already in the range of half the motor torque, which also depends on the temperature, the lubrication and the axial forces. In this case, in contrast to conventional machine test benches, the output power and efficiency can no longer be measured using speed and torque sensors. Hence, a calorimetric measurement method must be applied, which is explained in detail in **Sec. III**. In **Sec. IV**, the measurement results of the various motor designs, which were conducted with the test setup explained in **Sec. III**, are presented. Finally, the conclusions and an outlook are given in **Sec. V**.

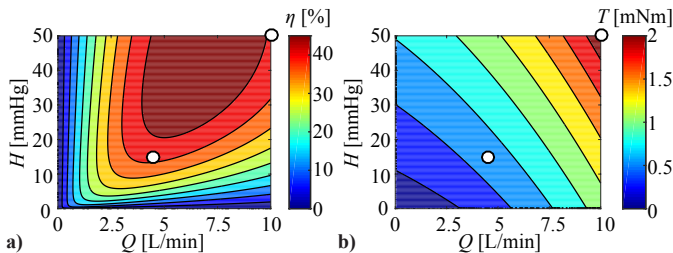


Fig. 3. a) Hydraulic efficiency and b) torque specifications per motor derived from the CFD based pump model investigated in [9]. The operating point for nominal and maximum load are also highlighted. The nominal and maximum rotational speed are 2800 rpm and 5500 rpm, respectively.

II. MOTOR OPTIMIZATION

The motor optimization bases on the mechanical design of the IBP concept for Fontan patients proposed in [9]. A cross section view of the optimized IBP concerning fluid dynamic and hemocompatibility aspects is shown in Fig. 2 and the already fixed corresponding dimensions are listed in Tab. I. In the following, the still freely selectable dimensions (cf. Fig. 4) and materials of the proposed axial flux permanent magnet (AFPM) synchronous machine are optimized step by step, starting with the impeller's magnetic design, i.e. the permanent magnets (PM), the number of pole pairs as well as the material and thickness of the back iron.

The rotor's magnetic design space inside the impeller is given by a ring volume with a maximum total height of $h_r = 2.5$ mm for the PM and the rotor back iron, as well as a maximum outer and minimum inner diameter of $d_{ro} = 18.2$ mm and $d_{ri} = 11.9$ mm, respectively. For the PM, the material Ni-48SH is selected, which is able to withstand the elevated temperatures used during the sterilization process of medical devices before implantation into the body and which still provides a high residual flux density of $B_r = 1.36$ T at 40°C . Furthermore, in order to minimize the thickness h_{rbi} of the rotor's back-iron material, VACOFLUX 50 is chosen, which is a machinable solid material that in addition features a high saturation flux density of up to 2.3 T.

Based on these materials, where also the non-linear magnetic characteristics are considered, now the optimal number of pole pairs p and the distribution between back-iron and PM thickness h_{pm} with the magnet to rotor thickness ratio $r_{pmr} = h_{pm}/(h_{pm} + h_{rbi})$ can be determined. This is done with 3D-FEM simulations, since the magnetic air gap, given by the impeller and pump-housing titanium walls with thicknesses of $h_{ti} = 0.4$ mm each (medical grade titanium, 6Al4V ELI) and the blood passage between the impeller and the pump housing of $h_b = 0.5$ mm, is large compared to the rotor dimensions, and leads to a strongly pronounced leakage flux, thus has to be taken into account in order to properly determine the flux distribution and saturation of the back-iron material. However, due to the large air gap, an exact dimensioning of the stator tooth and stator winding width w (cf. Fig. 4) is not needed yet in order to determine

TABLE I
MECHANICAL DIMENSIONS OF THE IBP SYSTEM ALREADY DEFINED BY FLUID DYNAMIC AND HEMOCOMPATIBILITY ASPECTS ANALYZED IN [9].

Dimension	Value
Max. Outer Rotor Diameter d_{ro}	18.2 mm
Min. Inner Rotor Diameter d_{ri}	11.9 mm
Max. Rotor Height h_r	2.5 mm
Titanium Wall Thickness h_{ti}	0.4 mm
Blood Passage Height h_b	0.5 mm
Min. Stator Inner Diameter d_{si}	11.5 mm

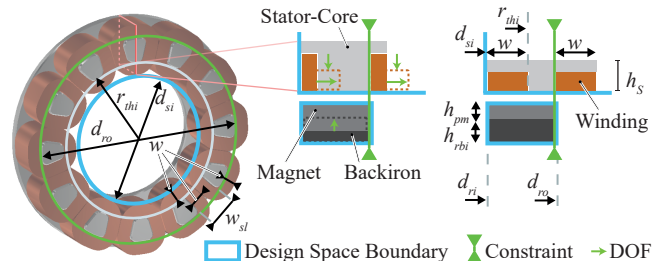


Fig. 4. Motor optimization design space according to Tab. I as well as the applied optimization constraints and degrees of freedom (DOF). Furthermore, geometric dimension definitions used for the optimization are shown.

the PM to rotor thickness ratio r_{pmr} . As will be shown later for the stator optimization, the stator winding width w can theoretically be varied between $w_{\text{min}} = 0$ mm and the smaller value of either

$$w_{\text{max,rad}} = \frac{(d_{\text{ro}} - d_{\text{si}})}{2}, \quad (1)$$

which is the maximum winding width in radial direction, or

$$w_{\text{max,ang}} = \frac{\pi d_{\text{si}}}{3p \cdot 2}, \quad (2)$$

corresponding to the maximum winding width in angular direction, which is found by dividing the inner rotor circumference by the number of stator teeth $3p$, while per stator tooth on all sides, i.e. two times, a distance of w is needed for the winding. For pole-pair numbers $p = 2 - 5$, the maximum winding width is always limited by (2) and varies between $w_{\text{max}} = 1.2 - 3.1$ mm. Hence, for all FEM simulations a feasible winding width value of $w = 1$ mm is used. It turns out that pole-pair numbers $p = 1$ and $p = 2$ lead to unnecessarily thick back iron, i.e. low PM to total rotor thickness ratio r_{pmr} . In combination with the given comparably large inner stator diameter d_{si} , pole-pair numbers $p = 1$ and $p = 2$ lead to unfavourable coil geometries with curvature angles greater than 180° , with related difficulties in the manufacturing process. Furthermore, $p = 1$ would also result in unbalanced radial forces, which means that $p = 1$ and $p = 2$ are omitted. On the other hand, with an increasing pole-pair number p , the thickness of the back iron can be reduced, i.e. r_{pmr} is increasing. However, pole-pair numbers more than four are considered as impractical due to the resulting very small stator tooth and stator winding width w in this application. Therefore, only the two pole-pair numbers $p = 3$ and $p = 4$ are investigated in this paper.

Fig. 5 illustrates the 3D-FEM simulation results for the amount of peak flux through one stator tooth, i.e. the main flux, normalized by the highest flux obtained with $p = 3$ with respect to the PM to rotor thickness ratio r_{pmr} . $r_{\text{pmr}} = 0$ means that no PM exists and therefore no flux is produced, while with $r_{\text{pmr}} = 1$, the total rotor height of $h_r = 2.5$ mm is occupied by the PM and no back iron exists, i.e. the flux is closing through the air. It can be noted that for both pole-pair numbers $p = 3$ and $p = 4$ a flat optimum around $r_{\text{pmr}} = 0.5 - 0.9$ is found, while actually at $r_{\text{pmr}} = 1$ the flux is still 87% for $p = 3$ and 91% for $p = 4$ of the respective peak flux. Hence, there would be the option to omit any back iron, however, 10% lower flux leads to 23% more conduction losses in the stator winding and since for the underlying application the losses are crucial, an optimal value of $r_{\text{pmr}} = 0.64$ ($h_{\text{pm}} = 1.6$ mm and $h_{\text{rbi}} = 0.9$ mm) is selected, such that the back-iron rings are still nicely manufacturable and mechanically stable.

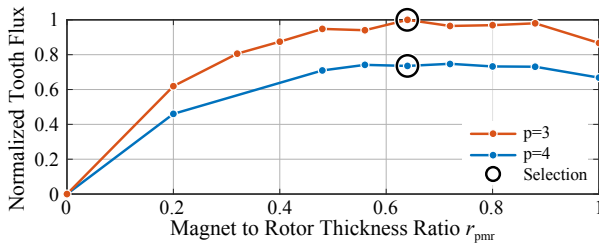


Fig. 5. Main flux linked with each stator tooth for $p = 3$ and $p = 4$ and normalized to the peak value obtained with $p = 3$ as a function of the permanent magnet (PM) to total rotor thickness ratio r_{pmr} . For the hardware prototypes an value of $r_{\text{pmr}} = 0.64$ ($d_{\text{pm}} = 1.6$ mm and $d_{\text{rbi}} = 0.9$ mm) was selected as marked by the circles.

In a second step, now the stator of the AFPM motors is optimized for the two pole-pair numbers $p = 3$ and $p = 4$. As shown in **Fig. 2**, the minimal inner stator diameter of $d_{\text{si}} = 11.5$ mm is defined by the pump inlet cross-section, which restricts the stator winding heads to not extend radially further inwards than the rotor's PMs. Furthermore, since the width of the winding head is equal to the winding width w , which is equal to half the slot width w_{sl} , if production tolerance related clearances are neglected, the slot width w_{sl} directly defines the inner radius of the stator tooth position r_{thi} . On the other hand, as shown in **Fig. 4**, the diameter limiting the radial dimension of the stator teeth is set equal to the outer rotor diameter r_{ro} as an optimization constraint, since if chosen smaller it would result in an unwanted decreasing stator flux linkage, however, if chosen larger, it would only increase the stator volume and winding resistance without substantially increasing the flux linkage. Hence, in the stator optimization, on the one hand only the winding width w is varied between $w_{\text{min}} = 0$ mm and the minimum value given by either (1) or (2), which also directly defines the stator tooth size, and on the other hand the total stator height h_s is varied, where the three discrete stator tooth lengths 1.1 mm, 2.1 mm and 3.1 mm are analyzed (cf. **Fig. 4**).

However, not only the limits of the geometric design space restrict the possible solutions, but also the selection of materials and related production process limitations especially for small machines, as present in this case, are crucial. For example, soft magnetic composite (SMC) materials (e.g. SOMALLOY 500) resulting in low core losses are restricted to a minimum realizable physical dimension of the stator geometry due to the material brittleness, and therefore cannot be used for the targeted application. In this paper, the application of soft magnetic steel (MG2, Valbruna GROUP) with good machinability properties is investigated, allowing thin back-iron and tooth geometries. Unfortunately, this comes with the cost of a lower electrical resistivity of $0.76 \Omega\text{mm}^2/\text{m}$ compared to $80 \Omega\text{mm}^2/\text{m}$ in SOMALLOY 500 leading to higher eddy current losses. However, in this specific application, the requirement of a reasonable manufacturing of the stator resulting in a minimal thickness of 0.7 mm is the decisive reason for this decision.

The stator optimization with respect to copper losses is again carried out with 3D-FEM simulations. In **Fig. 6 a**), the resulting copper losses P_{Cu} depending on the stator height h_s and winding width w for two assumed winding fill factors $ff = 0.4$ and $ff = 0.6$ are shown. There, a winding width of $w = 1.2$ mm is selected, which is close to the optima for all different p - h_s -combinations. As indicated in **Fig. 6 b**), the copper losses decrease with increasing winding height h_s as the current density in the winding decreases.

Based on the selected winding width $w = 1.2$ mm, now the achievable winding fill factor ff for an orthocyclic winding arrangement depending on the winding cross-section and the number of turns can be calculated, where also the stator core to winding and winding to winding clearance of $d_{\text{cl}} = 0.05$ mm as well as the maximum wire thickness including the insulation according to DIN 60317 is considered. As shown in **Fig. 7**, a winding fill factor in the range of $ff = 0.4 - 0.5$ can be achieved for this motors. Since the number of turns per coil of the stator winding N_{Coil} is an additional degree of freedom, N_{Coil} should be selected in such a way that a high winding fill factor ff and thus low losses are obtained, however, it should also result in a reasonable induced voltage which optimally matches to the electrical specifications of the power electronic inverter. To avoid driveline infections, powering the pump from a transcutaneous energy transfer (TET) system including a back-up battery, where an intermediate DC/DC-converter regulates the DC-link voltage, would

III. CALORIMETRIC TEST BENCH

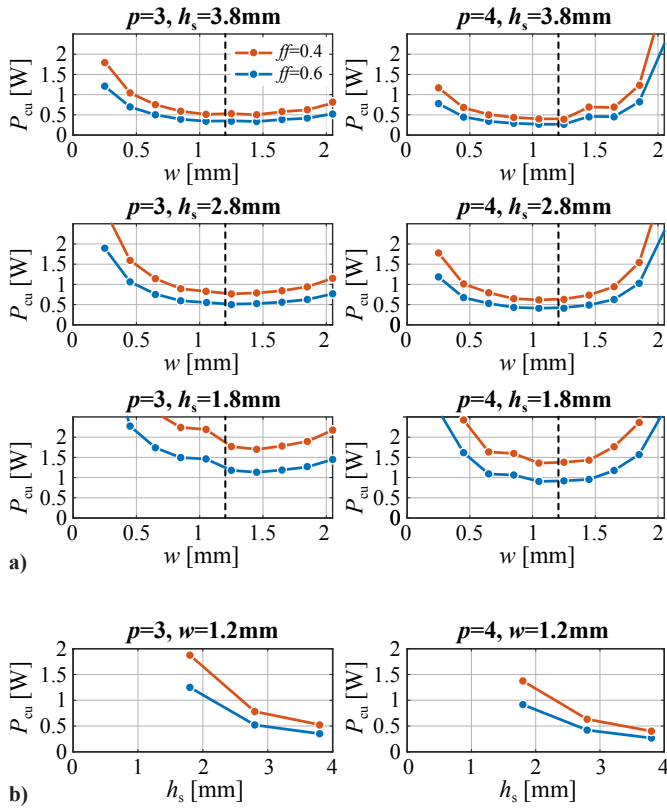


Fig. 6. a) Resulting copper losses P_{Cu} depending on the stator height h_s and winding width w for the two assumed winding fill factors $ff = 0.4$ and $ff = 0.6$. For all different p - h_s -combinations a winding width of $w = 1.2$ mm (indicated with vertical line) is selected which is close to all optima. b) Resulting copper losses for $w = 1.2$ mm depending on h_s .

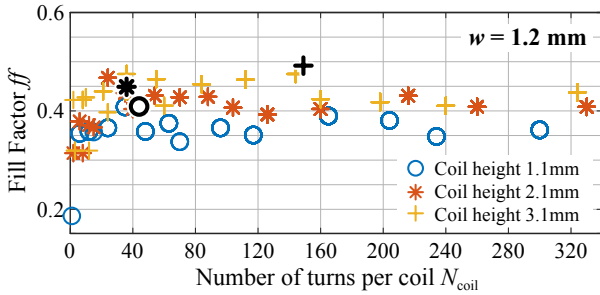


Fig. 7. Calculated achievable fill factors ff for an orthocyclic winding arrangement depending on the number of turns per coil N_{coil} and the winding cross-section defined by the nominal coil height (which includes mounting clearances of $d_{cl} = 0.05$ mm) and nominal coil width, where based on diameter information also the insulation thickness according to DIN 60317 standard is considered. The realized windings of the hardware prototypes are indicated in black.

be preferred. However, it increases complexity and development cost, which might be critical considering the comparably small market size. A lower limit to the nominal wire diameter d_{Cu} is given by the production process of an orthocyclic winding, which is assumed to be around 0.1 mm. The selected number of turns per coil N_{coil} , with maximum fill factor in the defined N_{coil} -range, depending on the different coil heights h_c and different pole pairs p as well as the RMS induced phase voltage constant obtained from simulation are given in **Tab. II** for the considered and realized stator concepts.

In order to verify the motor optimization, a test bench for the experimental performance quantification, i.e. the measurement of the motor losses has to be realized. Typically, the machine efficiency is determined by measuring the electrical input power at the three-phase terminal by current and voltage measurements, and by measuring the mechanical output power with a speed and torque sensor. In this application, however, the nominal machine torque of 2.2 mNm per motor is really low, which makes an accurate torque measurement seriously challenging. Even though sensors for measuring such low torques exist, the additional friction caused by e.g. the bearings - already generating half of the nominal machine torque - would falsify the measured result, especially due to the fact that the bearing friction cannot be calibrated since it strongly changes over time due to heat generation and lubrication characteristics. Furthermore, when either measuring high efficiencies (low relative losses) or small absolute losses, the measurement accuracy strongly deteriorates when two similar values, i.e. input and output power, are subtracted from each other. Therefore, instead of measuring the difference of input and output power, a calorimetric measurement principle, which directly measures the resulting motor losses, is applied. One approach to determine the motor losses, is e.g. to pump a liquid through the assembled final IBP system (cf. **Fig. 2**), while the flow rate and the fluid temperature difference between inlet and outlet is measured. However, the low flow rate as well as the very small bulk temperature difference of substantially less than the local hot-spot temperature limit of 2°C based on the specifications, lead to a limited accuracy due to e.g. the low relative temperature resolution of around 0.1°C . Furthermore, the measured losses would include the hydraulic losses of the pump, which are not negligible with a hydraulic efficiency of below 50% (cf. **Fig. 3**). Another option, as proposed in this paper, is to measure just the motor performance without pump characteristics by using a back-to-back configuration of a motor under test (MUT) and a load motor, where the two respective rotors are mounted on the same shaft and are axially separated in such a way that the MUT is placed in a thermally insulated box (10 mm thick transparent acrylic glass (PMMA)), while the bearings and the load motor are located outside the box as shown in **Fig. 8**. Hence, the loss measurement of the MUT is not affected by the bearing friction losses and the applied load can be controlled with the load machine by connecting different load resistors to the load machine's windings. There, the losses could be measured by first determining the thermal resistance of the box $R_{th,box}$ by calibration and then measure during machine operation the temperature difference between the temperature in the box T_{box} and the ambient temperature T_{amb} . In this case, however, for a fixed ambient temperature of e.g. $T_{amb} = 32^\circ\text{C}$ controlled by an oven (cf. **Fig. 8**), the resulting box temperature $T_{box} = R_{th,box} \cdot P_{MUT} + T_{amb}$ would linearly depend on the generated overall machine losses P_{MUT} and therefore would vary between each measurement point.

In order to measure the machine efficiency for realistic conditions, i.e. the motor is operated at a constant box temperature equal to an elevated body temperature of $T_{amb} = 40^\circ\text{C}$ where the PM already show a reduced magnet strength and the winding already features an increased winding resistance, the use of a balancing method is proposed [12]. There, the box is first heated up with an electrical resistor R_h , where a box temperature controller adjusts the DC current I_h (resulting in the heating power P_h) in such a way that a constant box temperature of $T_{box} = 40^\circ\text{C}$ is achieved. In addition, a fan circulates the air inside the box, maintaining constant thermal conditions. As soon as the temperature is stabilized, the MUT is

turned-on and is operated at a load converging to a constant level, while bearings are heating up and, if freshly lubricated (WD-40), lubrication conditions stabilize. Consequently, the generated motor losses would lead to a further temperature increase inside the box, however, the box temperature controller now reduces the injected current I_h into the resistor (resulting in heating power reduction ΔP_h) and keeps T_{box} constant. Hence, the motor losses are directly obtained with a high accuracy by measuring the DC voltage V_h and DC current I_h of the heating resistor.

It should be mentioned, that this measurement principle advantageously doesn't depend on the relative or absolute temperature accuracy of the temperature sensors as long as the box temperature controller always regulates to the same reference value. Furthermore, as long as the test bench setup remains unchanged, also the machine mounting or the shaft passing through the box wall leading to some leakage heat flux, don't deteriorate the measurement accuracy, since these effects can be compensated by increasing the resistor losses and by calibration as described in the following. The calorimetric test bench is calibrated by applying a DC current to the motor windings, while for the calculation of the injected DC power to the motor under test P_{MUT} , also the DC voltage drop directly across the winding terminals is measured. In addition, based on these DC values also the stator winding resistance can be determined as listed in **Tab. II**. The measured motor losses P_{MUT} are also cross-checked with the losses measured at the heating resistor P_h . As shown in **Fig. 9**, there is a linear mismatch between P_{MUT} and P_h that can be explained by the mentioned leakage flux through the machine mounting, which due to the different thermal coupling is not the same for the stator winding as for the heating resistance. Hence, a calibration factor $k_c = 1.1958$ has to be considered, which is captured based on a least squares approximation and results in a root mean square error (RMSE) of 0.0063 W for five loss measurements in the range of 0.1 W to 0.6 W.

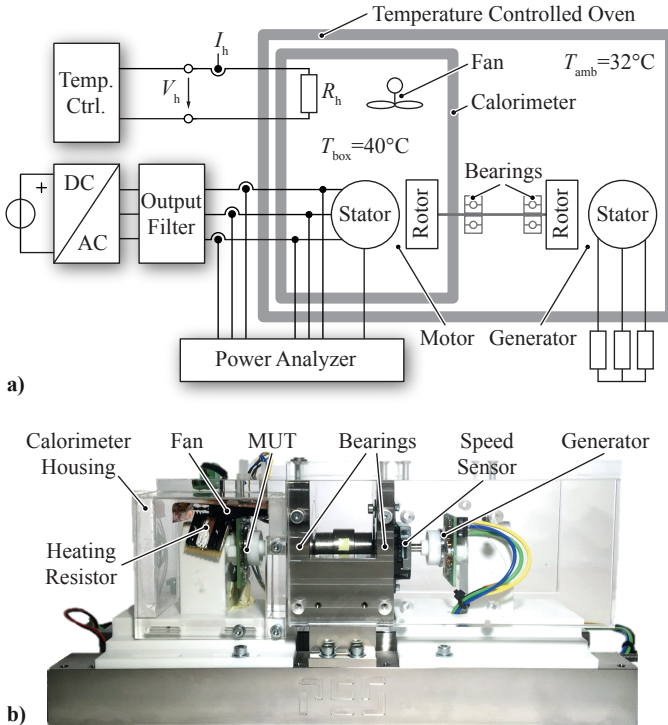


Fig. 8. a) Schematic of the applied calorimetric motor loss measurement test bench and b) picture of its realization in hardware.

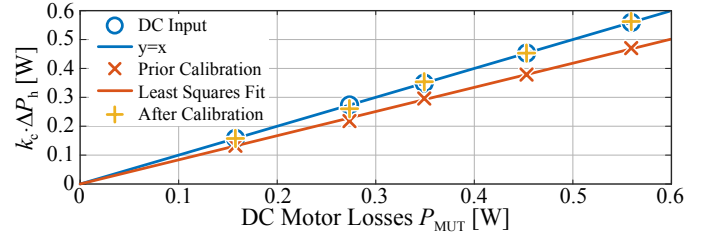


Fig. 9. Calibration results of the calorimetric test bench obtained by simultaneously measuring the injected DC power to the motor under test P_{MUT} and the loss reduction at the heating resistor ΔP_h , yielding the calibration factor $k_c = 1.1958$.

IV. EXPERIMENTAL RESULTS

Four motors with varying pole pair-number p and stator height h_s are realized as hardware prototypes. As an example, the motor P4H3.8 with $p = 4$ and $h_s = 3.8$ next to the titanium pump prototype parts is shown in **Fig. 10**.

In a first step, different motor parameters of all four motor realizations, like the DC stator winding resistance $R_{\text{Ph,Meas}}$ and the induced voltage while spinning the generator as a motor, are determined. In **Tab. II**, the different characteristics of the realized motor prototypes (P3H3.8, P4H3.8, P4H2.8 and P4H1.8) are summarized, while e.g. also the RMS induced phase voltage constant $k_{\text{Ind,Sim}}$ obtained from FEM simulations is compared to the measured value $k_{\text{Ind,Meas}}$. The relative error $e_{k_{\text{Ind}}}$ between the simulated and measured constant deviates within 4% and 17%. This includes, considering the small motor size, comparably large manufacturing and material tolerances as well as magnet tolerance governed clearances leading to smaller than expected realizable rotor back iron thickness with $h_{\text{rbi}} = 0.75$ mm compared to the ideal simulation value of $h_{\text{rbi}} = 0.9$ mm.



Fig. 10. Pump prototype parts: a) titanium housing and impeller of the implantable blood pump and b) stator and PM rotor of the motor prototype with a pole-pair number of $p = 4$ and a stator height of $h_s = 3.8$.

TABLE II
MOTOR CHARACTERISTICS OF ALL FOUR MOTOR PROTOTYPES.

Motor Parameter	Motor Prototype			
	P3H3.8	P4H3.8	P4H2.8	P4H1.8
Pole-Pair Number p	3	4	4	4
Stator Height h_s [mm]	3.8	3.8	2.8	1.8
Stator diameter d_{so} [mm]	20.6	20.6	20.6	20.6
Wire diameter d_{Cu} [mm]	0.125	0.125	0.2	0.125
Number of Turns/Coil N_{Coil}	148	149	36	44
$R_{\text{Ph,Meas}}$ [Ω]	8.95	9.4	0.935	2.89
$k_{\text{Ind,Sim}}$ [V/krpm]	0.633	0.764	0.178	0.204
$k_{\text{Ind,Meas}}$ [V/krpm]	0.607	0.641	0.149	0.171
$e_{k_{\text{Ind}}}$	4%	16%	17%	16%
$c_H \cdot 10^4$ [W · s]	1.66	3.84	2.72	2.02
$c_E \cdot 10^7$ [W · s ²]	8.19	1.86	2.34	0
RMSE(P_{ML}) [W]	0.041	0.030	0.078	0.030

After determining all motor parameters, the losses of the different motor realizations are measured with the calorimetric test bench described in the previous section. There, both stator and rotor are also covered with a 0.4 mm thick titanium wall (6Al4V ELI) emulating the housing of the real pump setup such that also possible eddy current losses caused by the housing are taken into account. The motors are operated with a three-phase inverter (DRV8301 with LAUNCHXL-F28027, Texas Instruments) featuring sensor-less field oriented control (Motorware, Texas Instruments). In order to be able to associate the measured motor losses P_{ML} to a certain input or output power, the electrical input power P_{In} (this includes the phase currents I_{Ph}) are measured with a power analyzer (WT 3000, YOKOGAWA) at the motor terminals, while the PWM inverter voltage ($f_s = 45$ kHz) is first low-pass filtered ($f_c = 10$ kHz) to obtain smooth machine voltages and currents. All different motors are tested at nominal load with $n_{nom} = 2800$ rpm and $T_{out,nom} = 0.62$ mNm ($P_{out,nom} = 0.18$ W) and at maximum load with $n_{max} = 5500$ rpm and $T_{out,max} = 2.2$ mNm ($P_{out,max} = 1.27$ W), corresponding to a blood flow of 4.5 L/min with a pressure head of 15 mmHg and a blood flow of 10 L/min with a pressure head of 50 mmHg, respectively. There, it must be mentioned that due to the time-varying behaviour of the bearing friction, which contributes up to 50–100% of the load torque, it was almost impossible to always operate the motors at the exactly same load torques. Especially due to the fact that the calorimetric measurements are very time-consuming, where the thermal equilibrium is reached after around two hours, it was not reasonable to readjust the load of the machine iteratively.

In **Tab. III** to **Tab. VI**, the experimental results for all four stator prototypes captured at different measurement points MP_1 to MP_3 are listed. With these results, now the residual losses $P_{ML,res}$, i.e. the high-frequency winding losses, the core losses or eddy current losses in the titanium housing, can be counted back where either based on the measured winding resistance $R_{Ph,Meas}$ and phase current I_{Ph} the winding losses are calculated and subtracted from the total machine losses P_{ML} as

$$P_{ML,res} = P_{ML} - 3 \cdot R_{Ph} \cdot I_{Ph}^2, \quad (3)$$

or where the mechanical output power $P_{out} = P_{in} - P_{ML}$ is subtracted from the inner machine output power, which is found based on the induced voltage $U_{Ind,Ph}$ and phase current I_{Ph} as

$$P_{ML,res} = 3 \cdot U_{Ind,Ph} \cdot I_{Ph} - (P_{in} - P_{ML}). \quad (4)$$

As can be noticed in **Tab. III** to **Tab. VI**, the two values obtained from (3) and (4) do not match exactly, which is caused by measurement errors occurring in the measurement of R_{Ph} , I_{Ph} and $U_{Ind,Ph}$. There, the effective resistance R_{Ph} is strongly temperature-dependent and the electric values I_{Ph} and $U_{Ind,Ph}$ are time-dependent and are at the lower measurement range of the used power analyzer. It should be mentioned, however, that the overall machine losses P_{ML} are measured with a high accuracy, since there the heating resistor's DC-values are measured with highly accurate multimeters.

Nevertheless, in general it can be stated that the total machine losses P_{ML} are not only defined by the winding losses, which means that especially the stator designs P3H3.8 and P4H3.8 with large stator height h_S result in a high percentage of residual losses, since there the current density and the winding losses are reduced, while on the other hand e.g. the core losses increase with larger core volume. In contrast, for the design with the smallest stator height P4H1.8, the residual losses are below 5% to 15%.

Based on the measured losses, now the expected machine losses for the whole operating range, i.e. a torque range of $T = 0 - 2.2$ mNm

TABLE III
EXPERIMENTAL RESULTS OF THE MOTOR PROTOTYPE P3H3.8

Motor Parameter	MP ₁	MP ₂	MP ₃
Rotational Speed n [rpm]	2500	2500	5500
Measured Phase Current I_{Ph} [A]	0.070	0.118	0.169
Measured Input Power P_{in} [W]	0.418	0.872	2.356
Measured Machine Losses P_{ML} [W]	0.189	0.480	1.081
Percentage of Residual Losses acc. (3)	31%	22%	29%
Percentage of Residual Losses acc. (4)	47%	30%	39%

TABLE IV
EXPERIMENTAL RESULTS OF THE MOTOR PROTOTYPE P4H3.8

Motor Parameter	MP ₁	MP ₂	MP ₃
Rotational Speed n [rpm]	2500	5500	5500
Measured Phase Current I_{Ph} [A]	0.061	0.096	0.146
Measured Input Power P_{in} [W]	0.378	1.209	2.075
Measured Machine Losses P_{ML} [W]	0.208	0.514	0.841
Percentage of Residual Losses acc. (3)	50%	50%	29%
Percentage of Residual Losses acc. (4)	59%	62%	37%

TABLE V
EXPERIMENTAL RESULTS OF THE MOTOR PROTOTYPE P4H2.8

Motor Parameter	MP ₁	MP ₂	MP ₃
Rotational Speed n [rpm]	2500	2500	5500
Measured Phase Current I_{Ph} [A]	0.368	0.419	0.591
Measured Input Power P_{in} [W]	0.654	0.774	2.285
Measured Machine Losses P_{ML} [W]	0.384	0.502	1.141
Percentage of Residual Losses acc. (3)	1%	2%	14%
Percentage of Residual Losses acc. (4)	37%	39%	27%

TABLE VI
EXPERIMENTAL RESULTS OF THE MOTOR PROTOTYPE P4H1.8

Motor Parameter	MP ₁	MP ₂	MP ₃
Rotational Speed n [rpm]	1500	2500	3700
Measured Phase Current I_{Ph} [A]	0.198	0.302	0.365
Measured Input Power P_{in} [W]	0.498	1.23	1.96
Measured Machine Losses P_{ML} [W]	0.390	0.848	1.281
Percentage of Residual Losses acc. (3)	13%	7%	10%
Percentage of Residual Losses acc. (4)	11%	1%	2%

and a rotational speed range of $n = 0 - 5500$ rpm corresponding to a blood flow range of $Q = 0 - 10$ L/min and a pressure head range of $H = 0 - 50$ mmHg, should be calculated, while also the residual loss of each machine should be taken into account. As already mentioned, the residual losses can be explained by high-frequency winding losses, core losses or eddy current losses in the titanium housing, while the hysteresis losses occurring in the core material are proportional to the angular frequency and the eddy current losses are increasing with the square of the angular frequency. Hence, the residual losses can be modelled as

$$P_{ML,res} = c_H \cdot \omega + c_E \cdot \omega^2 \quad (5)$$

where the coefficients c_H and c_E describe the hysteresis losses and the eddy current losses, while possible high-frequency losses in the windings are considered with both factors [13]. In addition, it is assumed that the flux density for each stator prototype is mainly defined by the PM magnetic flux density and therefore for each machine is constant, thus (5) only depends on the rotational speed ω . Accordingly, based on (3) to (5) and $P_{out} = T \cdot \omega$, the motor efficiency η can be calculated as

$$\eta = \frac{T\omega}{T\omega + 3R_{Ph,Meas} \left[\frac{T + c_H + c_E\omega}{3k_{Ind,Meas} \frac{60}{2\pi \cdot 1000}} \right]^2 + c_H\omega + c_E\omega^2}. \quad (6)$$

In a second step, for each motor design, the coefficients c_H and c_E are determined with non-negative (only positive coefficients have a physical meaning) least squares approximation (MATLAB, MathWorks), which are listed in **Tab. II**. Furthermore, the model-based motor losses are compared with the measured motor losses of each prototype by calculating the root mean square error (RMSE) at each measurement point MP, which is in the range of 0.030 – 0.078 W (cf. **Tab. II**) and thus proves the good matching between motor model and measured losses.

In **Fig. 11**, the calculated motor efficiency η and the motor losses P_{ML} for all four motor designs over the whole operating range ($T = 0 - 2.2$ mNm and $n = 0 - 5500$ rpm) are illustrated. In addition, also the different measurement points MP_x listed in **Tab. III** to **Tab. VI** are shown as triangles. The efficiency decrease close to the T -axis is related to copper losses while close to the n -axis to the residual losses. Hence, the slope of the iso-loss curves indicates the speed dependency and therefore the influence of the residual losses, e.g. for the machine P4H1.8, the flat iso-loss curves indicate a small contribution of the residual losses.

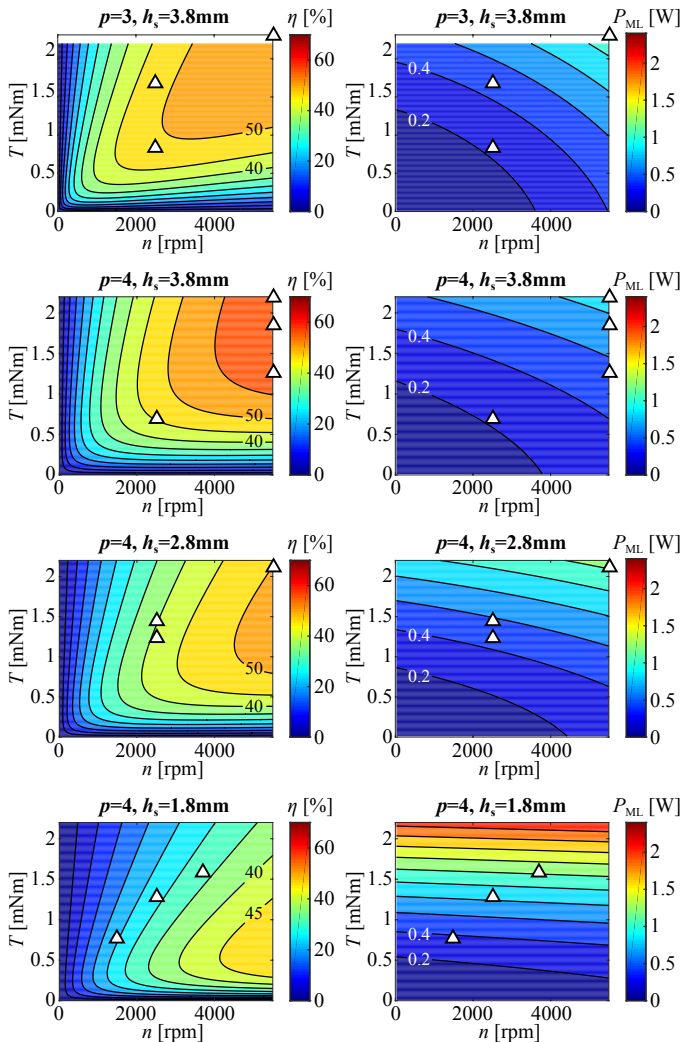


Fig. 11. a) Measurement-based motor efficiency and b) motor losses over the whole operating range for all four realized motor prototypes according to (6). In addition, also the different measurement points MP_x listed in **Tab. III** to **Tab. VI** are shown.

Concerning the loss distribution of the total motor losses, it should also be mentioned that the model not only allows to quantify the amount of the residual losses $P_{ML,res}$, but it also shows that due to the large share of $P_{ML,res}$, also additional stator winding losses $P_{cu,res}$ are generated. Hence, the copper losses can be divided into copper losses which occur if no core losses are present P_{cu} , i.e. copper losses caused by the current needed to produce torque,

$$P_{cu} = 3R_{Ph} \left[\frac{2\pi 1000}{3k_{Ind, Meas} 60} \right]^2 T^2 \quad (7)$$

and into additional copper losses $P_{cu,res}$, which occur due to the higher current need caused by the residual losses

$$P_{cu,res} = 3R_{Ph} \left[\frac{2\pi 1000}{3k_{Ind, Meas} 60} \right]^2 [(T + c_H + c_E \omega) - T]^2 \quad (8)$$

The corresponding loss distribution of all four motors gained with the measurement-based motor model for nominal load and for full load are shown in **Fig. 12**. As can be noticed, for the same stator height, $p = 4$ shows a slightly better performance compared to $p = 3$. Furthermore, since all motors produce less than 2.5 W of losses at full load, all motors can be employed for the space-critical application, which means that concerning volume a stator height of $h_S = 1.8$ mm should be preferred. However, if a TET-System is selected to power the pump, it may be beneficial to reduce the motor losses at the cost of a larger motor volume to increase battery lifetime. Additionally, if the power electronics shall be integrated into the pump, a small stator will be preferred regarding volume, but the additional inverter losses need to be considered as well.

Finally, the combination of the motor characteristics derived in this paper together with the CFD derived pump efficiency model from [9] allows to calculate the overall IBP system efficiency over the whole operating range. Due to the dominating lower pump efficiency, the

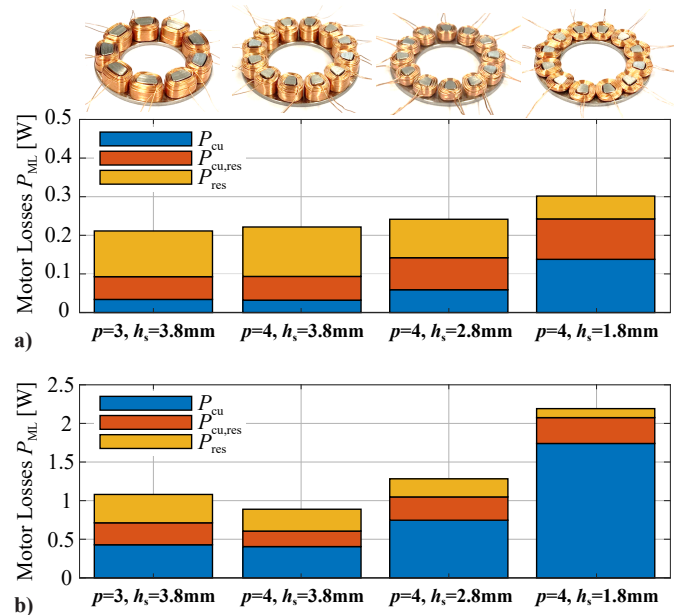


Fig. 12. Loss distribution between residual losses $P_{ML,res}$, copper losses P_{cu} caused by the current to produce torque and additional copper losses $P_{cu,res}$ caused by the residual losses for all four motor prototypes a) at nominal load, corresponding to a blood flow of 4.5 L/min and a pressure head of 15 mmHg, and b) at maximum load, corresponding to a blood flow of 10 L/min and a pressure head of 50 mmHg.

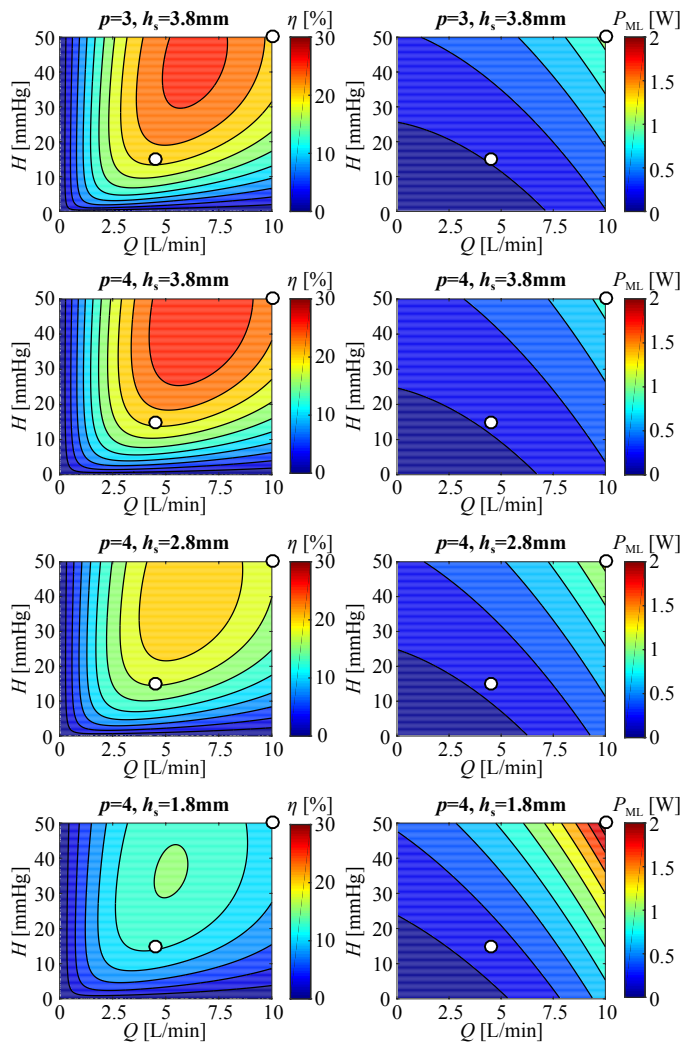


Fig. 13. **a)** Efficiencies of the measurement-based motor models combined with the hydraulic pump efficiency model from [9] and **b)** motor loss approximations over the whole operating range for all four realized motor prototypes.

shape of the system efficiency shown in **Fig. 13** is qualitatively similar to the pump efficiency as shown in **Fig. 3**. The highest local blood temperature increase at the wall adjacent to the motor is much higher than the bulk blood temperature increase [9]. Therefore only the motor losses are thermally relevant. **Fig. 13** shows the motor losses in function of blood flow Q and pressure head H and demonstrates that the motor losses increase exponentially with Q as well as with H . Therefore, the extreme conditions highly determine the minimal realizable motor size. However, considering the operating point with highest H and Q always as the thermally most critical one, must not be valid for all pumps, since the temperature increase also depends on the cooling flow, and in this specific case on the leakage blood flow [9].

V. CONCLUSION

In this paper, a constrained optimization and calorimetric experimental analysis of low torque axial flux permanent magnet motors for an implantable blood pump to support patients with a Fontan circulation is shown. In the rotor, the distribution between magnets and back-iron size, in the stator between winding and core volume

was optimized for varying stator heights and pole pair numbers of $p = 3$ and $p = 4$. The number of turns was optimized with respect to the achievable fill factor. Four motors with stator heights from 3.8 mm to 1.8 mm were realized as hardware prototypes. The loss measurement of this motors is not possible with conventional torque sensors. To enable the experimental analysis of the motor losses, a calorimetric test bench was established and calibrated with injection and measurement of DC power in the motor windings. For all four realized motors, the amount of non-copper residual losses was determined and a measurement based motor model derived for the analysis of motor losses and efficiency, as well as the system efficiency incorporating the hydraulic pump properties over the whole operating range. All four motors passed the ISO 14708-1 thermal requirements. The results reveal that the additional height contribution of the motors to the implant height can be reduced from 7.6 mm (62 %) to 3.6 mm (30 %). The future work will focus on the integration of the motor into the pump prototype, especially dealing with the challenges associated with the final ceramic contact bearings.

ACKNOWLEDGMENT

The authors thank Panteleimon Papamanolis and Morris Heller for their valuable inputs for the calorimetric measurement.

REFERENCES

- [1] F. Fontan and E. Baudet, "Surgical repair of tricuspid atresia," *Thorax*, vol. 26, no. 3, pp. 240–248, 1971.
- [2] P. Khairy, S. M. Fernandes, J. E. Mayer, J. K. Triedman, E. P. Walsh, J. E. Lock, and M. J. Landzberg, "Long-Term Survival, Modes of Death, and Predictors of Mortality in Patients with Fontan Surgery," *Circulation*, vol. 117, no. 1, p. 85, 2008.
- [3] M. Gewillig, "The Fontan Circulation," *Heart*, vol. 91, no. 6, pp. 839–846, 2005.
- [4] Y. d'Udekem, A. J. Iyengar, J. C. Galati, V. Forsdick, R. G. Weintraub, G. R. Wheaton, A. Bullock, R. N. Justo, L. E. Grigg, G. F. Sholler *et al.*, "Redefining Expectations of Long-Term Survival after the Fontan Procedure: Twenty-Five Years of Follow-Up from the Entire Population of Australia and New Zealand," *Circulation*, vol. 130, no. 11, pp. S32–S38, 2014.
- [5] P. W. O'Leary, "Prevalence, Clinical Presentation and Natural History of Patients with Single Ventricle," *Progress in Pediatric Cardiology*, vol. 16, no. 1, pp. 31–38, 2002.
- [6] A. L. Bui, T. B. Horwich, and G. C. Fonarow, "Epidemiology and Risk Profile of Heart Failure," *Nature Reviews Cardiology*, vol. 8, no. 1, pp. 30–41, 2011.
- [7] J. J. Han, M. A. Acker, and P. Atluri, "Left Ventricular Assist Devices: Synergistic Model Between Technology and Medicine," *Circulation*, vol. 138, no. 24, pp. 2841–2851, 2018.
- [8] C. R. Broda, D. A. Taylor, and I. Adachi, "Progress in Experimental and Clinical Subpulmonary Assistance for Fontan Circulation," *The Journal of Thoracic and Cardiovascular Surgery*, vol. 156, no. 5, pp. 1949–1956, 2018.
- [9] M. Granegger, B. Thamsen, E. J. Hubmann, Y. Choi, D. Beck, E. V. Buechel, M. Voutat, M. Schweiger, M. Meboldt, and M. Hübler, "A long-term Mechanical Cavopulmonary Support Device for Patients with Fontan Circulation," *Medical Engineering & Physics*, 2019.
- [10] A. Pohlmann and K. Hameyer, "Design of an BLDC Drive with Iron Core to Improve the Efficiency of Ventricular Assist Devices," in *Proc. of the IEEE International Conference on Electrical Machines and Systems (ICEMS)*, Busan, South Korea.
- [11] M. Kleinheyder, D. L. Timms, N. A. Greatrex, T. Masuzawa, O. H. Frazier, and W. E. Cohn, "Pulsatile Operation of the BiVACOR TAH-Motor Design, Control and Hemodynamics," in *Proc. of the IEEE 36th Annual International Conference of the IEEE Engineering in Medicine and Biology Society*.
- [12] P. Papamanolis, F. Krismer, and J. W. Kolar, "Minimum Loss Operation of High-Frequency Inductors," in *Proc. of the IEEE Applied Power Electronics Conference and Exposition (APEC)*.
- [13] H. Jordan, "Die ferromagnetischen Konstanten für schwache Wechselfelder," *Elektr. Nach. Techn.*, vol. 1, no. 8, 1924.